v-p material point method for weakly compressible problems☆

Zhen-Peng Chen[a], Xiong Zhang[a,*], Kam Yim Sze[b], Lei Kan[a], Xin-Ming Qiu[a]

[a] *School of Aerospace Engineering, Tsinghua University, Beijing 100084, PR China*
[b] *Department of Mechanical Engineering, University of Hong Kong, Pokfulam, Hong Kong, PR China*

ARTICLE INFO

ABSTRACT

The weakly compressible material point method (WCMPM) suffers from volumetric-locking and numerical oscillation in modeling fluid flow and fluid-structure interaction problems. In this paper, a *v-p* formulation of the material point method (*vp*-MPM) is proposed for weakly compressible problems based on a two-field variational principle. As only the velocity $\boldsymbol{v}$ and the pressure p are the independent variables, the *v-p* formulation has much less extra variables than those based on the Hu-Washizu multi-field variational principle which takes the velocity, strain and stress as independent variables. The pressure is assumed independently in the control volume of each gird node. Spurious pressure oscillation reduces but still occurs at the interface of discontinuity due to large pressure gradient difference across the interface. Therefore, a slope limiter is employed to suppress the oscillation and the general interpolation functions are used to eliminate the cell-crossing error. In order to extend the method to the fluid-structure interaction problems, the *v-p* formulation is incorporated into the improved coupled finite element material point method. Several numerical examples are presented to validate the *vp*-MPM.

© 2018 Elsevier Ltd. All rights reserved.

1. Introduction

As one of meshfree/particle methods, the material point method (MPM) proposed by Sulsky et al. [1–3] employs a set of Lagrange particles, which move through a predefined Eulerian background grid, to discretize the field variables in the material domain. At the beginning of each time step, the mass and momentum of particles are mapped to the grid to construct the information at the grid points. After solving the momentum equations on the background grid, the solutions are mapped from the grid points to the particles to update their positions and velocities. In the next time step, a new regular grid which encloses all particles is defined. Thus, mesh distortion associated with the Lagrangian finite element method (FEM) are completely eliminated.

Recently, the MPM has been used to study weakly compressible flows [4–8] and incompressible flows [9–11]. Li et al. [4] first proposed a weakly compressible material point method (WCMPM) by employing the weakly compressible equation of state (EOS). However, the weakly compressible EOS used in the WCMPM leads to significant spurious pressure oscillations and shortens the critical time steps. To overcome these shortcomings of the WCMPM, Zhang

et al. [9,10] proposed an incompressible material point method (iMPM) by employing the operator splitting technique to split the solution of momentum equation into two steps. An intermediate velocity field is first obtained from the momentum equations with the pressure term ignored, and then corrected by the pressure term to obtain a divergence-free velocity field. Kularathna and Soga [11] also proposed a similar scheme in almost the same time. The iMPM successfully eliminates the spurious pressure oscillations and significantly lengthens the critical time step yet its implementation is much more complicated than the WCMPM. For fluid flow problems with shocks, the fluid has to be considered as compressible which can not be modeled by the iMPM. Furthermore, it is difficult to obtain a converged solution for strong fluid-structure interaction (FSI) problems with extreme large deformation using an implicit formulation. To better model these kinds of problems, WCMPM needs further improvement to eliminate the spurious pressure oscillations.

In the WCMPM, two main factors leading to the pressure oscillations are the well known cell-crossing error [12] and volumetric locking [7]. Throughout this paper, node refers to grid point and cell refers to grid cell. To overcome the cell-crossing error, the generalized interpolation material point method (GIMP) was proposed by Bardenhagen et al. [12]. Inspired by the GIMP, many improved algorithms arise such as the contiguous particle GIMP (cpGIMP) [13], convected particle domain interpolation (CPDI) [14,15], dual domain material point (DDMP) [16] method and B-spline MPM
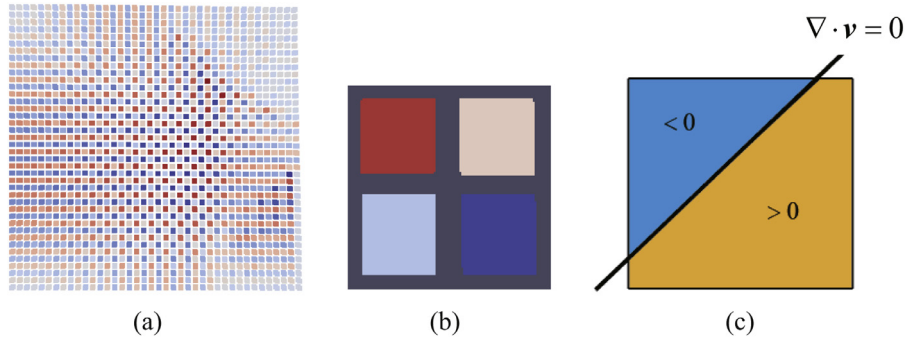
Fig. 1. Pressure oscillation observed in the WCMPM results.

[17,18], not to mention all. A common feature of these methods is the smoothed gradient of the interpolation function. Another kind of method to reduce the cell-crossing error is to use Gaussian quadrature instead of particle quadrature. Beuth et al. applied Gaussian quadrature to solve quasi-static problems in the implicit MPM [19], but still used particle quadrature at boundaries. Sulsky et al. [20] reconstructed the information at the nodes and Gaussian points using the moving least squares method (MLS) which makes the second-order accuracy possible for large deformation problems with fixed boundaries aligned with the grid boundaries.

Volumetric locking is more dominant than the cell-crossing error in the WCMPM and leads to inaccurate and non-physical predictions. The concept of volumetric locking initially came up in the finite element method (FEM) when modeling incompressible or nearly incompressible problems. A fully integrated element leads to excessive constraints placed on an element's deformation, causing the element to behave too stiffly. The MPM also suffers from volumetric locking because of large number of integrating points (particles) normally placed in each cell to reduce the quadrature error. Neither GIMP nor CPDI alleviates the pressure instability.

Strong oscillations have been observed in the pressure distribution in nearly incompressible flow problems simulated with the WCMPM, as shown in Fig. 1(a). By carefully examining Fig. 1(a), we can find that the pressure field distributes in a checkerboard pattern, as shown in Fig. 1(b). In the WCMPM, the velocity filed is approximated by bilinear polynomials, so that the divergence of velocity which is related to the incremental volumetric strain is linear in each element. Thus, the zero divergence divergence contour $\nabla \cdot \boldsymbol{v} = 0$ is a line in each element. Consequently, $\nabla \cdot \boldsymbol{v}$ will be negative in one side of the line and positive in another side, as shown in Fig. 1(c), leading to the checkerboard patter in pressure distribution.

Mast et al. [7] employed the standard trilinear interpolation functions with anti-locking techniques based on the Hu-Washizu multi-field variational principle [21]. In their algorithm, particles are treated as sample points for the approximation whilst the strain and stress at nodes/cells are constructed with the assumed trilinear or constant distribution. The reconstructed strain and stress of nodes/cells are then used to smooth the particle strains and stresses. The algorithm is able to mitigate the accumulation of fictitious strains and stresses, and significantly improves results for all field variables.

This paper aims to provide an efficient anti-locking algorithm for the WCMPM based on a two-field variational principle. The main hurdle in the applying the "standard" displacement formulation to incompressible or nearly incompressible problems lies in the determination of the mean stress or pressure which is related to the volumetric part of the strain. Thus, it is convenient to separate the pressure from the total stress field and treat it as an independent variable. A two-field variational principle where both

the displacement $\boldsymbol{u}$, or velocity $\boldsymbol{v}$, and the pressure p are the independent variables [22] has much less extra variables than the Hu-Washizu multi-field principle which also treat stress and strain as the independent variables.

In our v-p formulation, the pressure is reconstructed independently in the control volume of each node. Spurious oscillations will occur at the interface of discontinuity due to large pressure gradient difference between control volumes. To suppress the oscillations, a slope limiter is employed whilst the GIMP is adopted to eliminate the cell-crossing error. Moreover, the $v - p$ formulation has also been incorporated into the improved coupled finite element material point method (ICFEMP) [5,6,8] to suppress the spurious pressure oscillation encountered in FSI problems, and the resulted method is abbreviated as the vp-ICFEMP.

The remaining part of this paper is organized as follows. Section 2 reviews the WCMPM briefly. Section 3 presents the vp-MPM with the detailed implementation summarized in Section 4. Several numerical examples dealing with elastic wave propagation, dam break, wedge falling and water column impact on an elastic obstacle are studied in Section 5 to evaluate the accuracy, efficiency and accuracy of the proposed vp-MPM. Finally, the conclusions are summarized in Section 6.

2. Weakly compressible material point method

In this section, the equations governing the motion and deformation of fluid are first presented in the updated Lagrangian frame. Particles are employed to discretize the problem domain in the weak form so that the discrete momentum equations are established.

2.1. Governing equations

In material domain Ω, the momentum equations in the updated Lagrangian frame are given by

$$\boldsymbol{\sigma} \cdot \nabla + \rho \boldsymbol{b} = \rho \dot{\boldsymbol{v}} \tag{1}$$

where ∇ denotes the vector differential operator, $\boldsymbol{\sigma}$ is the Cauchy stress, ρ is the current density, $\boldsymbol{b}$ is the body force per unit mass, $\boldsymbol{v}$ is the velocity, the superimposed dot denotes the time derivatives. The boundary conditions are

$$(\boldsymbol{\sigma} \cdot \boldsymbol{n})|_{\Gamma_t} = \bar{\boldsymbol{t}}$$
$$\boldsymbol{v}|_{\Gamma_v} = \bar{\boldsymbol{v}} \tag{2}$$

where $\boldsymbol{n}$ is the unit outward normal to the boundary, Γ_v and Γ_t denote the prescribed displacement boundary and traction boundary of the domain Ω, respectively.

The weak form equivalent to the momentum equation and the traction boundary condition can be formulated as

$$\int_{\Omega} \rho \dot{\boldsymbol{v}} \delta \boldsymbol{v} \mathrm{d}\Omega + \int_{\Omega} \boldsymbol{\sigma} : \nabla \delta \boldsymbol{v} \mathrm{d}\Omega - \int_{\Omega} \rho \boldsymbol{b} \delta \boldsymbol{v} \mathrm{d}\Omega - \int_{\Gamma_t} \bar{\boldsymbol{t}} \delta \boldsymbol{v} \mathrm{d}\Gamma = 0 \tag{3}$$
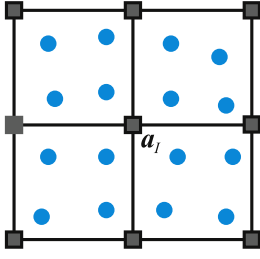
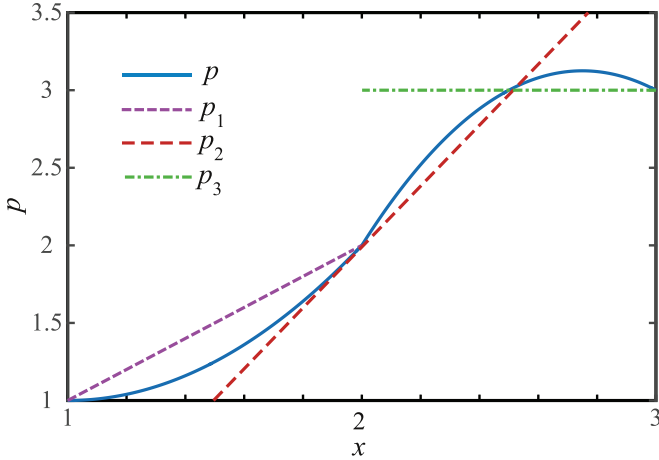**Fig. 2.** The support of node I for determining the unknown coefficients a_I.

Fig. 3. The smoothed pressure for an one-dimensional case.

where δv denotes the test function (virtual velocity) and the displacement boundary conditions must be satisfied a priori.

2.2. The weakly compressible equation of state

The fluid stress can be decomposed into two parts, namely,

$$\boldsymbol{\sigma} = p\boldsymbol{I} + \boldsymbol{\tau} \qquad (4)$$

where p is the fluid pressure, $\boldsymbol{I}$ represents the unit tensor and $\boldsymbol{\tau}$ signifies the viscous stress, respectively.

In the WCMPM [4], the pressure is updated by the weakly compressible equation of state (EOS)

$$p = -K\varepsilon_V = -K\boldsymbol{m}^{\mathrm{T}}\boldsymbol{\varepsilon} \qquad (5)$$

where $K = \rho_0 c^2$ is the bulk modulus with c denoting the artificial sound speed and ρ_0 denoting the reference density, ε_V and $\boldsymbol{\varepsilon}$ denote the volumetric strain and the strain in Voigt format, respectively, and

$$\boldsymbol{m}^{\mathrm{T}} = \begin{bmatrix} 1 & 1 & 1 & 0 & 0 & 0 \end{bmatrix} \qquad (6)$$

Morris et al. [23] estimated the artificial sound speed by

$$c^2 \sim \max\left(\frac{V_0^2}{\delta}, \frac{\nu V_0}{L_0 \delta}, \frac{bL_0}{\delta}\right) \qquad (7)$$

where V_0 is the flow velocity, b is the body force per unit mass, L_0 is the characteristic length, ν is the kinematic viscosity coefficient and

$$\delta = \frac{\Delta\rho}{\rho} \qquad (8)$$

represents the density fluctuation. Normally, $\delta \leq 3\%$.

2.3. MPM Scheme

In the MPM, the material domain is discretized by a set of particles. The velocity $\boldsymbol{v}$ of a point $\boldsymbol{X}$ is interpolated from the nodal velocity $\boldsymbol{v}_I$ and its gradient $\nabla\boldsymbol{v}$ is derived accordingly, i.e.

$$\boldsymbol{v}_p = \sum_{I=1}^{n_g} N_{Ip}\boldsymbol{v}_I, \qquad \nabla\boldsymbol{v}_p = \sum_{I=1}^{n_g} \nabla N_{Ip}\boldsymbol{v}_I \qquad (9)$$

where n_g is the total number of grid nodes, N_{Ip} and ∇N_{Ip} are the values of the interpolation function N_I of node I and its gradient evaluated at the location of particle p, respectively.

In the MPM, the particle quadrature is employed to integrate the weak form. Substituting Eq. (9) into Eq. (3) and invoking the arbitrariness of $\delta\boldsymbol{v}_I$ lead to

$$m_I\dot{\boldsymbol{v}}_I = \boldsymbol{f}_I \qquad I = 1, 2, \dots, n_g \qquad (10)$$

where

$$m_I = \sum_{p=1}^{n_p} N_{Ip}m_p \qquad (11)$$

is the lumped nodal mass and m_p is the mass of particle p,

$$\boldsymbol{f}_I = \boldsymbol{f}_I^{\mathrm{ext}} + \boldsymbol{f}_I^{\mathrm{int}} \qquad (12)$$

is the nodal force,

$$\boldsymbol{f}_I^{\mathrm{int}} = -\sum_{p=1}^{n_p} \frac{m_p}{\rho_p}\boldsymbol{\sigma}_p \cdot \nabla N_{Ip} \qquad (13)$$

is the internal nodal force,

$$\boldsymbol{f}_I^{\mathrm{ext}} = \sum_{p=1}^{n_p} m_p N_{Ip}\boldsymbol{b}_p \qquad (14)$$

is the external nodal force with the traction $\bar{\boldsymbol{t}}$ omitted for simplicity, and $\boldsymbol{b}_p = \boldsymbol{b}(\boldsymbol{x}_p)$.

The original MPM employs the trilinear C^0 interpolation functions N_I for computational efficiency. The discontinuity of the gradient of N_I leads to the cell-crossing error. The Generalized Interpolation Material Point (GIMP) method [12] developed by Bardenhagen et al. can significantly alleviate the cell crossing error and has been further improved by other authors [13–16]. In these GIMP-type methods, the C^0 interpolation function N_I and its gradient ∇N_I are replaced by a general interpolation function S_I and its gradient ∇S_I, respectively.

2.4. Volumetric locking in the WCMPM

The formulation of the MPM is similar to the traditional finite element method (FEM). Thus, shortcomings of the FEM are inherited by the MPM. The volumetric locking is the most notable shortcoming when the FEM is used to model nearly incompressible media such as rubbers, water and metals undergoing plastic flow. The volumetric locking results from the selection of the standard trilinear functions, which is unable to reproduce the correct deformation modes [24]. Presently, multi-field variational principles, high order interpolation and selective reduced integration are the most common anti-locking techniques employed in the FEM [22,24,25]. The similar concepts are applicable to the MPM. On the other hand, Mast et al. [7] pointed out that the high order shape functions such as GIMP, CPDI, B-spline cannot alleviate the volumetric locking. Therefore, the standard linear shape functions were employed with anti-locking techniques based on the Hu-Washizu multi-field variational principle [7]. The formulation is able to mitigate the accumulation of fictitious strains and stresses, and significantly improves the predictions of all the field variables.
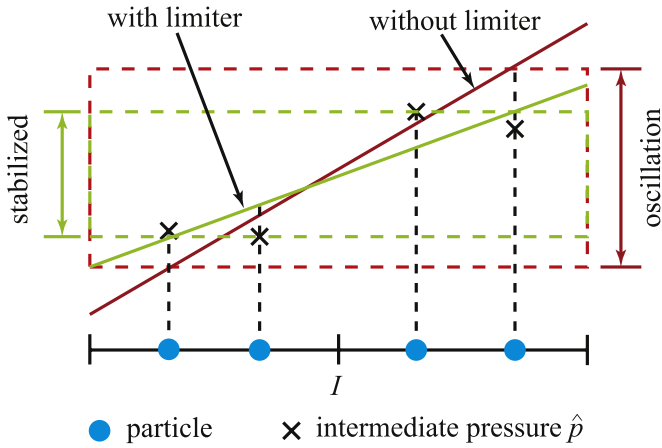
Fig. 4. The linear pressure field in the support of node I with and without a limiter. (For interpretation of the references to color in this figure, the reader is referred to the web version of this article.)
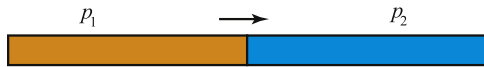

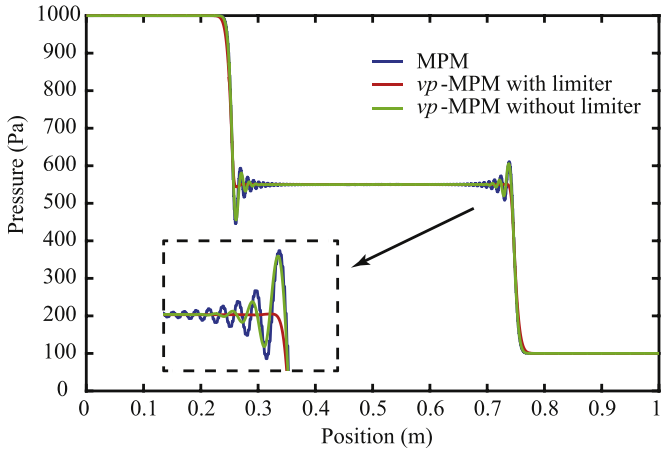**Fig. 5.** The propagation of a 1D elastic wave.

Fig. 6. The pressure distribution at $t = 5$ ms.

In order to explain the volumetric locking, Eq. (10) are rewritten in matrix form as

$$\boldsymbol{M\ddot{u}} + \boldsymbol{Ku} = \boldsymbol{f} \tag{15}$$

where $\boldsymbol{u}$ is the nodal displacement vector, $\boldsymbol{f}$ is the nodal force vector, $\boldsymbol{M}$ is the mass matrix,

$$\boldsymbol{K} = K \sum_p^{n_p} \boldsymbol{B}^{\mathrm{T}}(\boldsymbol{mm}^{\mathrm{T}})\boldsymbol{B}V_p \tag{16}$$

is the stiffness matrix, V_p is the volume of particle p, $\boldsymbol{B}$ is the strain matrix evaluated at $\boldsymbol{x}_p$. Note worthily, the rank of $\boldsymbol{B}^{\mathrm{T}}(\boldsymbol{mm}^{\mathrm{T}})\boldsymbol{B}$ is equal to one.

In the weakly compressible flows, the bulk modulus K is large and can be viewed as the penalty parameter. For each cell, the rank of the element stiffness matrix is equal to the number of the integration points n_e. The solvability of Eq. (15) requires the whole stiffness matrix $\boldsymbol{K}$ to be singular, which is equivalent to

$$n_p = \sum_e n_e < n_u \tag{17}$$

where n_u is the number of degree of freedoms (DOFs) of the system. The particle spacing is commonly set to one half of the cell size. Obviously, the number of particles n_p is far more than the total DOFs of nodes, n_u, and results in the volumetric locking and the pressure instability. Furthermore, only employing high order or smoothed shape functions (GIMP, the B-spline function, etc.) without increasing the number of nodes can not mitigate the volumetric locking, which agrees with the conclusion of Mast et al. [7].

3. *vp*-MPM for weakly compressible problems

In the FEM, the application of a mixed formulation can alleviate the volumetric locking which plagues the computational analysis of nearly incompressible media encountered in a variety of engineering problems in ranging from soil mechanics to aerospace engineering [22]. The identical problem also occurs in incompressible fluid flows. Many of the existing FEM strategies make use of multi-field variational principles such as the well-known Hu-Washizu multi-field variational principle [21].

Mast et al. [7] employed the standard trilinear shape functions with anti-locking techniques based on the Hu-Washizu multi-field variational principle with three independent fields (displacement, stress and strain). In the nearly incompressible problems, using the two-field principle in which the displacement $\boldsymbol{u}$, or velocity $\boldsymbol{v}$, and the pressure p are the independent variables is more convenient [22]. The main problem in the application of a "standard" displacement formulation to incompressible or nearly incompressible problems lies in the determination of the mean stress or pressure which is related to the volumetric strain. Hence, it is convenient to separate the pressure from the total stress field and treat it as an independent variable. In the v-p formulation, only one extra variable needs to be reconstructed, while in the Hu-Washizu multi-field formulation, 12 extra variables have to be reconstructed.

3.1. The v-p formulation

In the mixed formulation, we take the velocity $\boldsymbol{v}$ and the pressure p as the independent variables. The weak form (3) can be rewritten by treating p as an independent variable as

$$\int_\Omega \rho \dot{\boldsymbol{v}} \delta \boldsymbol{v} \mathrm{d}\Omega + \int_\Omega \boldsymbol{\tau} : \nabla \delta \boldsymbol{v} \mathrm{d}\Omega - \int_\Omega p \nabla \cdot \delta \boldsymbol{v} \mathrm{d}\Omega - \int_\Omega \rho \boldsymbol{b} \delta \boldsymbol{v} \mathrm{d}\Omega$$
$$- \int_{\Gamma_t} \bar{\boldsymbol{t}} \delta \boldsymbol{v} \mathrm{d}\Gamma = 0 \tag{18}$$

In addition, a weak form of Eq. (5) should be imposed, namely

$$\int_\Omega \left(\boldsymbol{\varepsilon}_V + \frac{p}{K} \right) \delta p \mathrm{d}\Omega = 0 \tag{19}$$

which represents the constitutive law.

3.2. The pressure approximation

The v-p formulation takes the velocity and pressure as unknown variables. In the v-p formulation of MPM, the velocity field is constructed by the nodal interpolation, which is the same as the standard MPM. To approximate the pressure field, the trial function and test function are chosen to be linear functions, i.e.

$$p(\boldsymbol{x}, t) = \boldsymbol{q}^{\mathrm{T}}(\boldsymbol{x})\boldsymbol{a}(t) \tag{20}$$

$$\delta p(\boldsymbol{x}, t) = \delta \boldsymbol{a}^{\mathrm{T}}(t)\boldsymbol{q}(\boldsymbol{x}) \tag{21}$$

where $\boldsymbol{q} = (1, x, y, z)^{\mathrm{T}}$ is the linear polynomial basis and $\boldsymbol{a} = (a_0, a_1, a_2, a_3)^{\mathrm{T}}$ is the coefficient vector to be determined. The local linear pressure approximation (20) resembles the variable reconstruction used in the finite volume method (FVM) to construct variable fields in each element. The undetermined coefficient vector $\boldsymbol{a}$ can be determined by particles (nodes in
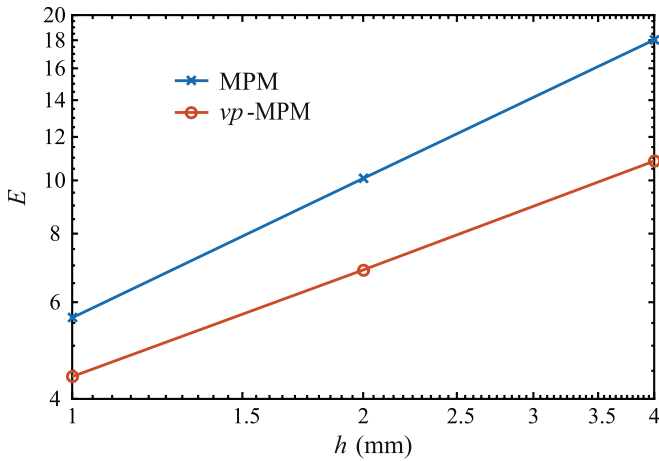
Fig. 7. The $\log E - \log h$ curve with different cell sizes.
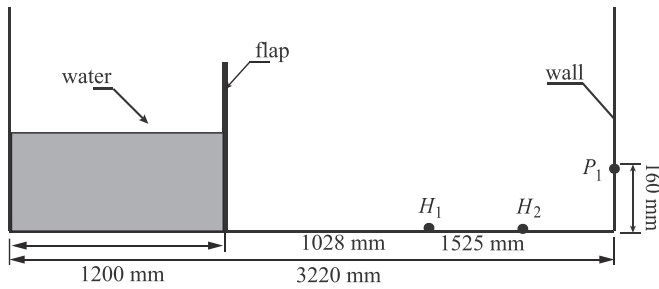

Fig. 8. The schematic of dam break.

the FVM) in a chosen stencil, which will be discussed in more detail below. The second-order approximation can be achieved by employing $\boldsymbol{q} = (1, x, y, z, x^2, xy, y^2, yz, z^2, xz)^T$, and $\boldsymbol{a} = (a_0, a_1, a_2, a_3, a_4, a_5, a_6, a_7, a_8, a_9)^T$.

Substituting Eqs. (20) and (21) into Eq. (19) and invoking the arbitrariness of $\delta\boldsymbol{a}$ results in

$$\int_\Omega \boldsymbol{q}\boldsymbol{q}^T d\Omega \boldsymbol{a} = \int_\Omega \boldsymbol{q}\hat{p} d\Omega \tag{22}$$

where

$$\hat{p} = -K\varepsilon_V \tag{23}$$

is the intermediate pressure.

Eq. (22) provides a way to obtain the smoothed pressure at sample point $\boldsymbol{x}$. In the standard MPM, the pressure information is stored in the particles. Thus, a straightforward idea is to smooth the pressure by evaluating Eq. (22) at each particle, where the coefficient vector $\boldsymbol{a}$ is defined at the particles. For example, to determine the coefficient vector $\boldsymbol{a}_s$ of particles s, Eq. (22) can be rewritten as

$$\int_{\Omega_s} \boldsymbol{q}\boldsymbol{q}^T d\Omega \boldsymbol{a}_s = \int_{\Omega_s} \boldsymbol{q}\hat{p} d\Omega \tag{24}$$

where Ω_s is the local approximation domain of particle s. By employing the particle quadrature in Eq. (24), the coefficient vector $\boldsymbol{a}_s$ can be obtained as

$$\boldsymbol{a}_s = \boldsymbol{H}_s^{-1} \sum_{p=1}^{n_s} \boldsymbol{q}_p \hat{p}_p V_{sp} \tag{25}$$

where

$$\boldsymbol{H}_s = \sum_{p=1}^{n_s} \boldsymbol{q}_p \boldsymbol{q}_p^T V_{sp} \tag{26}$$
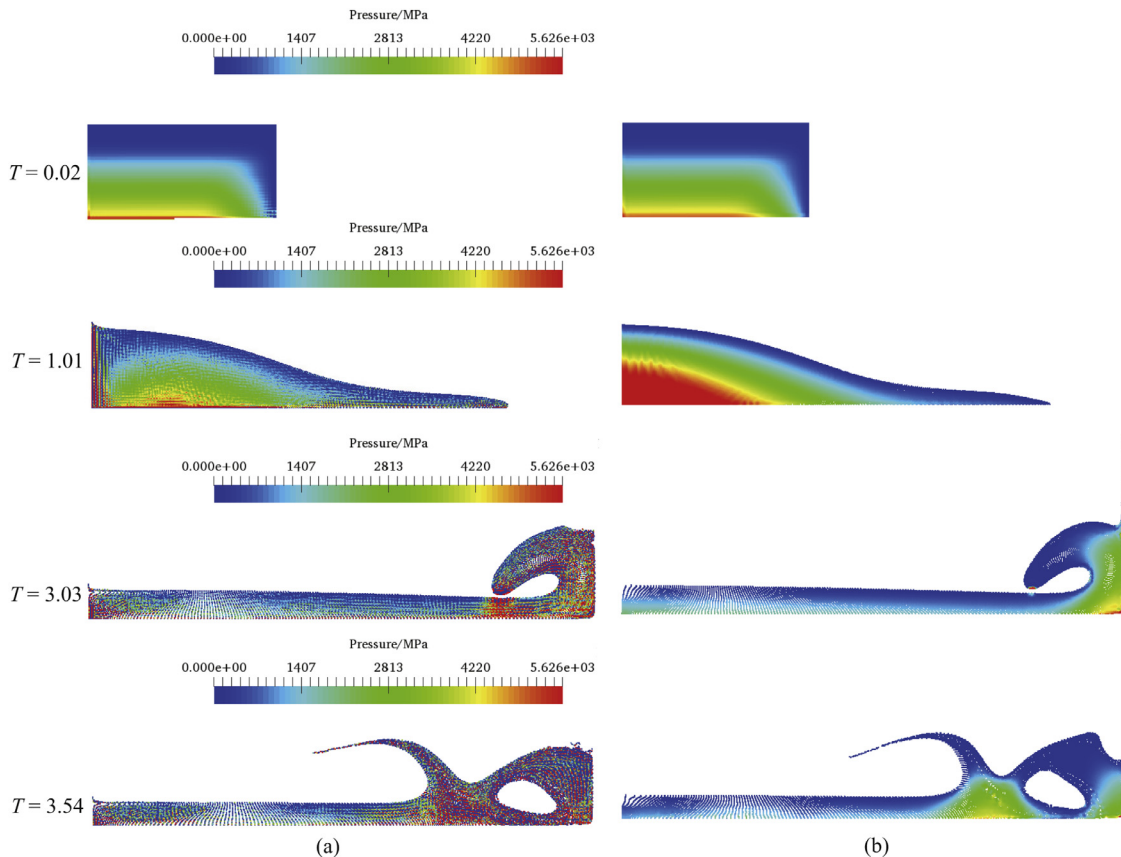

Fig. 9. Dam break configurations obtained by the (a) WCGIMP and (b) vp-GIMP.
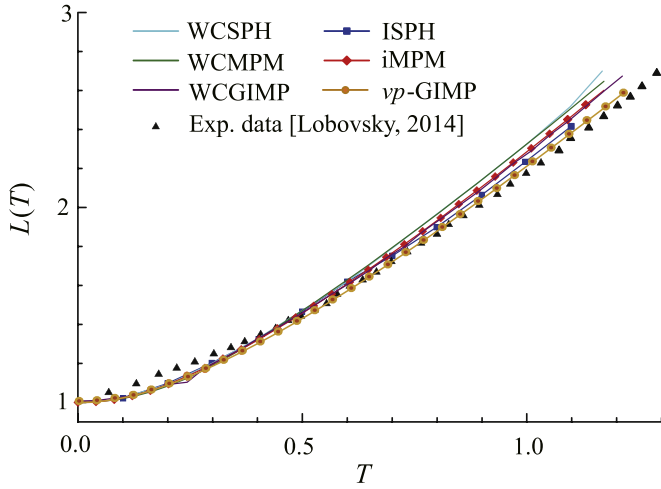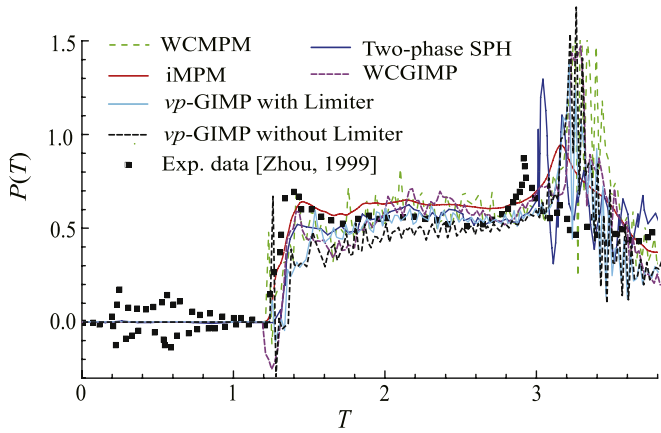
Fig. 10. Time evolution of the water front.

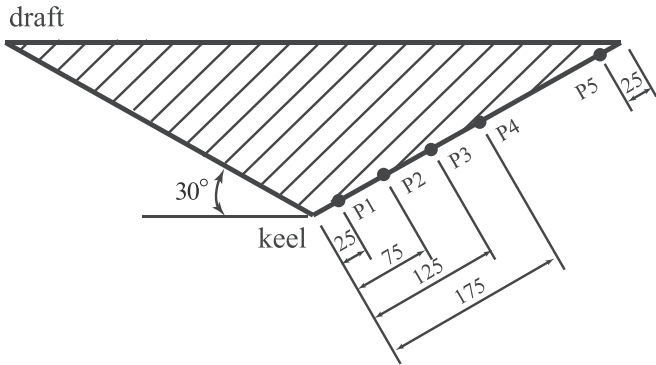**Fig. 11.** Time evolution of the pressure at location P_1.

Fig. 12. The section of wedge [36].

is a 4×4 matrix, n_s represents the number of particles in the local approximation domain Ω_s of particle s, $V_{sp} = W_s(\boldsymbol{x}_p)V_p$ is the control volume of particle s contributed by particle p with V_p denoting the volume of particle p. The function $W_s(\boldsymbol{x})$ is a partition of unity, i.e. $\sum_s W_s(\boldsymbol{x}) = 1$, which defines the local approximation domain of particle s, i.e. $\Omega_s = \{\boldsymbol{x} : W_s(\boldsymbol{x}) \neq 0, \sum_s W_s(\boldsymbol{x}) = 1\}$. Note that the local approximation domains of particles overlap each other, i.e. $\bigcup \Omega_s \neq \Omega$, but the partition of unity makes $\sum_s V_{sp} = V_p$. Any continuous function satisfying the partition of unity condition can be used to define the local approximation domain of a particle. In

this study, the grid nodal shape function $N_I(\boldsymbol{x})$ is used to define the local approximation domain of node I, which will be discussed in more detail below.

The above strategy is very similar to the moving least square (MLS) technique. However, it increases the computational cost significantly because the inversion of a 4×4 matrix is required at every particle. Besides, it requires the neighbor particles searching, which is also very expensive. To maintain the computational efficiency of the WCMPM, Eq. (22) can be evaluated only at the node or cell centroid. The former and the latter are termed as the node-based approach and the cell-based approach, respectively [7]. Once the pressure values at nodes or cell centroids are obtained, those at the particles are interpolated from the nodes in the node-based approach, or is directly set to be the value of the cell centroid of the cell containing the particle in the cell-based approach. The cell-based approach uses the particles in the same cell as the sample points to approximate the cell pressure. Though the cell-based approach can mitigate the volumetric locking, it is ineffective for reducing the pressure oscillation because the assumed pressure distribution is not continuous across the cell boundary. On the contrary, the node-based approach secures a continuous pressure and, thus, is employed in this article.

In the node-based approach, the pressure distribution is assumed to be linear in the support domain of each node. The support domain of node I is defined as $\Omega_I = \{\boldsymbol{x}|N_I(x) > 0$ with $N_I(\boldsymbol{x})$ denoting the shape function of node I, as shown in Fig. 2 [7]. The trial and test functions are chosen to be Eq. (20) and Eq. (21), respectively. The polynomial coefficients in $\boldsymbol{a}_I = (a_0, a_1, a_2, a_3)^\mathrm{T}$ of node I is determined using the particles within the support of node I.

Mast et al. evaluated Eq. (22) by particle quadrature in the support of node I defined by the interpolation function $N_I \neq 0$. Thus,

$$\boldsymbol{a}_I = \boldsymbol{H}_I^{-1} \sum_p^{n_p} N_{Ip} V_p \boldsymbol{q}_{Ip} \hat{p}_p \tag{27}$$

where

$$\boldsymbol{H}_I = \sum_p^{n_p} N_{Ip} V_p \boldsymbol{q}_{Ip} \boldsymbol{q}_{Ip}^\mathrm{T} = \sum_p^{n_p} N_{Ip} V_p \begin{bmatrix} 1 & x_p & y_p & z_p \\ x_p & x_p^2 & x_p y_p & x_p z_p \\ y_p & x_p y_p & y_p^2 & y_p z_p \\ z_p & x_p z_p & y_p z_p & z_p^2 \end{bmatrix} \tag{28}$$

The node-based approach is efficient because Eq. (27) is only evaluated at nodes and the neighbor particles searching is no more needed. After solving the coefficient vector $\boldsymbol{a}_I$ from Eq. (27), the pressure of particles can be obtained by interpolating the nodal values to the particles, i.e.

$$p_p = \sum_I N_{Ip} \boldsymbol{q}_p^\mathrm{T} \boldsymbol{a}_I \tag{29}$$

It should be noted that the smoothed pressure in Eq. (29) is not linear. Take the one-dimensional case shown in Fig. 3 as an example. The pressure fields of node 1 ($x_1 = 1$), node 2 ($x_2 = 2$) and node 3 ($x_3 = 3$) are chosen as $p_1(x) = (x - 1) + 1$, $p_2(x) = 2(x - 2) + 2$ and $p_3(x) = 3$, respectively. The smoothed pressure p obtained from Eq. (29) is plotted in Fig. 3, which is piecewise quadratic and continuous at nodes.

Finally, the volume of particles is updated according to the weakly compressible EOS as

$$V_p = V_0\left(1 + \varepsilon_{iip}\right) = V_0\left(1 - \frac{p_p}{K}\right) \tag{30}$$

3.3. Slope limiter

The pressure is reconstructed independently in the control volume of each node in a way similar to the reconstruction step in
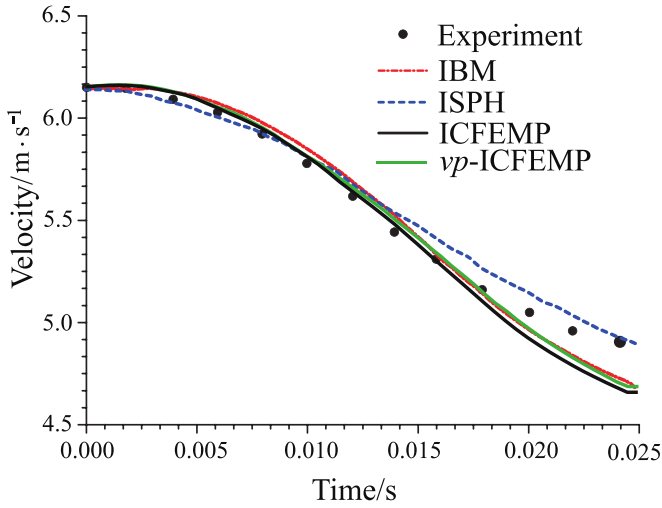
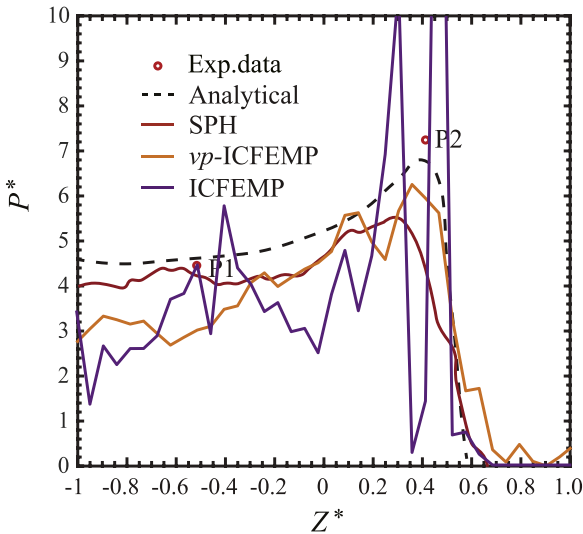**Fig. 13.** The time history of the vertical velocity.

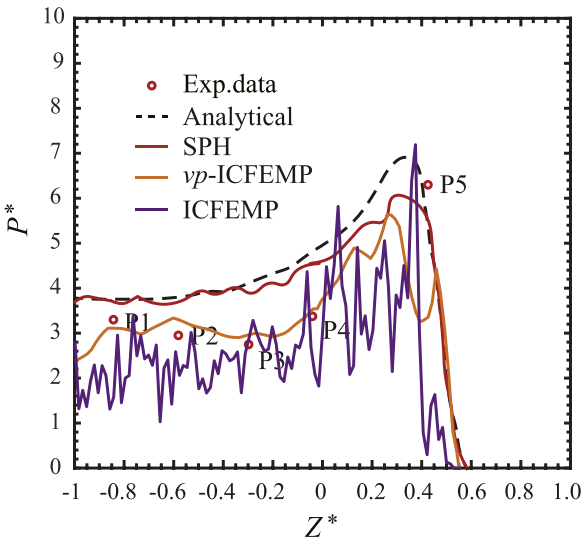**Fig. 14.** Comparisons of pressure results at $t = 0.00435$ s.

Fig. 15. Comparisons of pressure results at $t = 0.0158$ s.

the finite volume method (FVM). In addition to the checkerboard pattern spatial oscillation caused by the volumetric locking, large pressure gradient difference between control volumes will also result in spurious oscillation in pressure near the interface of discontinuity. Thus, a slope limiter, also known as gradient limiter, to limit the gradients of the reconstructed function [26–28] can be employed to suppress the spurious oscillation. A limiter first computes the trial gradient, and then reduces it by a scalar $\phi \in [0, 1]$, which is applied to variables reconstruction. One of the most famous slope limiter was introduced by Barth and Jespersen [29].

A slope limiter can be readily implemented in the vp-MPM. The coefficients a_1, a_2 and a_3 corresponding to the pressure gradient determined from Eq. (27) are multiplied by the limiter $\phi \in (0, 1)$ to define the adjusted pressure field for node I, i.e.

$$\tilde{p}(\boldsymbol{x}) = \tilde{p}_0 + \phi a_1 (x - \bar{x}) + \phi a_2 (y - \bar{y}) + \phi a_3 (z - \bar{z}) \tag{31}$$

where

$$\bar{x} = \left(\sum_{p=1}^{n_p} x_p V_p \right) \Big/ \left(\sum_{p=1}^{n_p} V_p \right)$$

$$\bar{y} = \left(\sum_{p=1}^{n_p} y_p V_p \right) \Big/ \left(\sum_{p=1}^{n_p} V_p \right)$$

$$\bar{z} = \left(\sum_{p=1}^{n_p} z_p V_p \right) \Big/ \left(\sum_{p=1}^{n_p} V_p \right)$$

are the coordinates of the centroid of the particles that influence node I,

$$\tilde{p}_0 = a_0 + a_1 \bar{x} + a_2 \bar{y} + a_3 \bar{z}$$

is the pressure at the centroid $(\bar{x}, \bar{y}, \bar{z})$. For clarity, the nodal subscript I is omitted in above equations. As the limiter ϕ varies from 0 to 1, the hyperplane $\tilde{p}(\boldsymbol{x}, \phi)$ will rotate around the centroid $(\bar{x}, \bar{y}, \bar{z})$. If $\phi = 1$ (not limited), Eq. (31) is equal to the original reconstructed pressure. We do not use the origin (0,0,0) as the rotation center, because if particle p is far away from the origin, even a small difference of ϕ will induce a large change in pressure at $\boldsymbol{x}_p$ and fail the slope limiter. The slope limiter ϕ can be determined by

$$p^{\min} = \min_{p \in \Omega_I} \{p_p\} \leqslant \tilde{p}(\boldsymbol{x}) \leqslant \max_{p \in \Omega_I} \{p_p\} = p^{\max} \tag{32}$$

where Ω_I signifies the stencil used in the reconstruction. A popular limiter, Barth limiter [29] defined as

$$\phi_I = \min_{p \in \Omega_I} (\phi_{Ip}), \quad \phi_{Ip} = \min(1, r_{Ip}) \tag{33}$$

is employed here, where

$$r_{Ip} = \begin{cases} \dfrac{f^{\max} - f_I}{\nabla f \cdot (\boldsymbol{x}_p - \boldsymbol{x}_c)} & \nabla f \cdot \boldsymbol{x}_p > 0 \\ \dfrac{f^{\min} - f_I}{\nabla f \cdot (\boldsymbol{x}_p - \boldsymbol{x}_c)} & \nabla f \cdot \boldsymbol{x}_p < 0 \\ 1 & \nabla f \cdot \boldsymbol{x}_p = 0 \end{cases} \tag{34}$$

The stencil Ω_I is chosen to be the set consists of all particles covered by the control volume of node I, i.e.

$$\Omega_I = \{p \mid N_{Ip} > 0\} \tag{35}$$

Once the slope limiter is obtained, the adjusted pressure field will be used to smooth particles' pressure. Fig. 4 plots the linear pressure field in the support of node I with and without a limiter in one dimension. The red line shows the pressure field without a slope limiter. When applying a slope limiter, the gradient of pressure is restricted, leading to a reduction in the amplitude of pressure oscillation, as illustrated by the green line. The pressure oscillation is suppressed after employing a slope limiter.
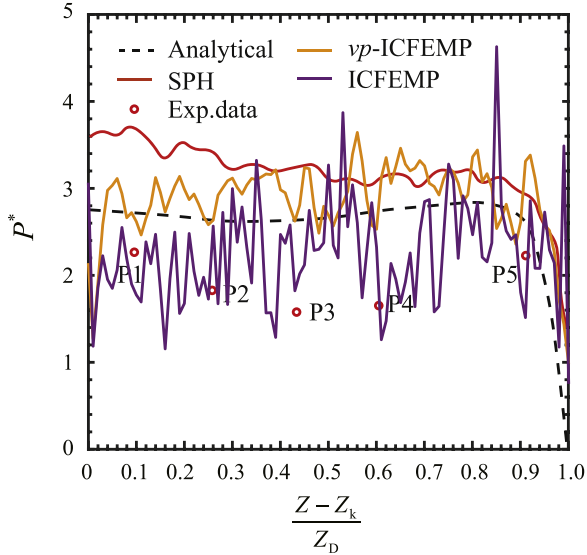
Fig. 16. Comparisons of pressure results at $t = 0.0202$ s.

4. Numerical implementation

The detailed implementation of the vp-MPM in a time step can be summarized as follows.

1. At the beginning of the time step t^n, establish the background grid that encloses all particles and initialize the nodal mass by Eq. (11) and the nodal momentum by

$$\boldsymbol{p}_I^{n-1/2} = \sum_{p=1}^{n_p} N_{Ip} m_p \boldsymbol{v}_p^{n-1/2} \qquad (36)$$

respectively.

2. Calculate the intermediate pressure $\hat{p}$ of particles by Eq. (23), which is the same as the standard WCMPM.
3. Determine the nodal pressure coefficient vector $\boldsymbol{a}_I$ by Eq. (27) with the slope limiter Eq. (32), and store the polynomial coefficients.
4. Smooth the pressure of particles by Eq. (29) and update the volume of particles by Eq. (30).
5. Calculate the nodal force using Eq. (12), and integrate the momentum equation (10) to update the nodal momentum $\boldsymbol{p}_I^{n+1/2}$.
6. Update the particle velocity $\boldsymbol{v}_p^{n+1}$ and position $\boldsymbol{x}_p^{n+1}$ by

$$\boldsymbol{v}_p^{n+1/2} = \boldsymbol{v}_p^{n-1/2} + \Delta t^n \sum_I^{N_g} N_{Ip}^n \boldsymbol{f}_I^n / m_I^n \qquad (37)$$

$$\boldsymbol{x}_p^{n+1} = \boldsymbol{x}_p^n + \Delta t^{n+1/2} \sum_{I=1}^{N_g} N_{Ip}^n \boldsymbol{p}_I^{n+1/2} / m_I^n \qquad (38)$$

where $\Delta t^{n+1/2} = t^{n+1} - t^n$, $\Delta t^n = t^{n+1/2} - t^{n-1/2} = \frac{1}{2}(\Delta t^{n-1/2} + \Delta t^{n+1/2})$.

If the GIMP is used with the $v - p$ formulation, the interpolation function N_I should be replaced by the GIMP interpolation function S_I in all above equations except in Eqs. (27)–(29).

5. Numerical examples

5.1. Elastic wave propagation

The first example is an elastic wave propagation for validating the accuracy of the vp-MPM. Fig. 5 shows two 1D water columns each of length 0.5 m separated by a flap. The initial pressures of the left and right columns are $p_1 = 1000$Pa and $p_2 = 100$Pa, respectively. The weakly compressible EOS with density $\rho = 1000$kg/m^3 and artificial sound speed $c = 50$ m/s is assumed

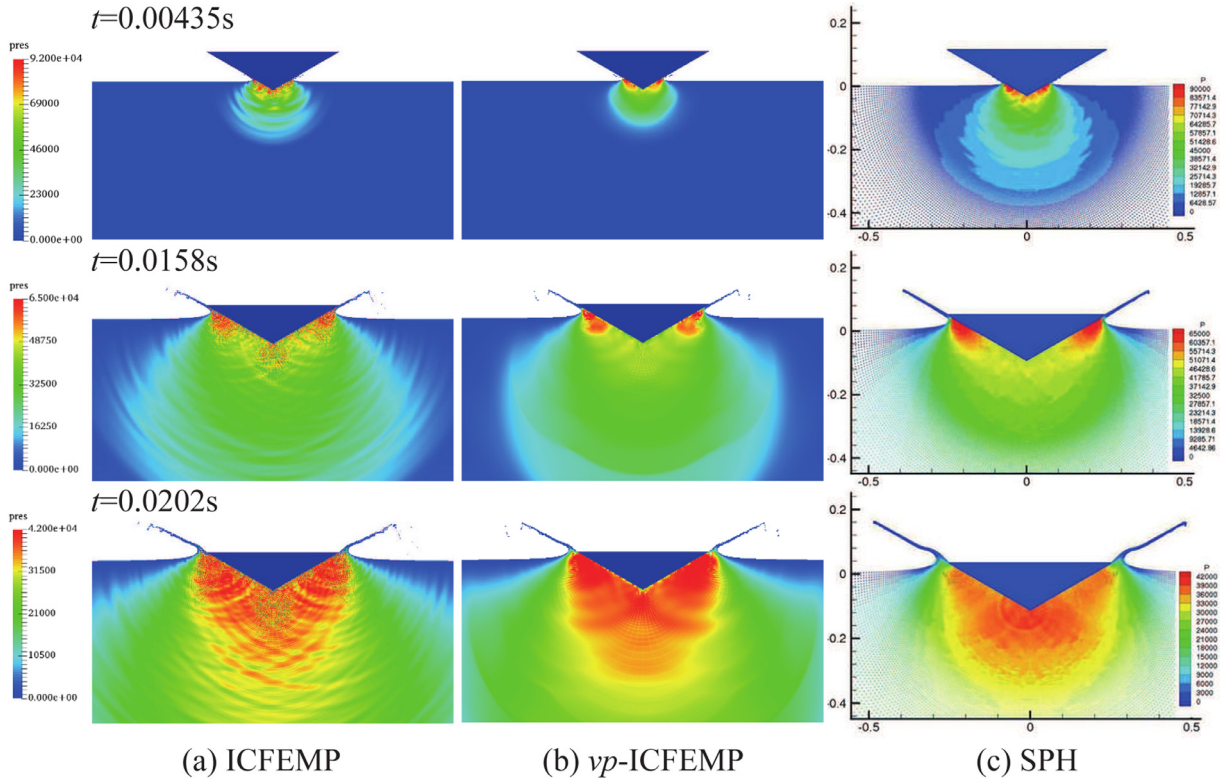(a) ICFEMP   (b) vp-ICFEMP   (c) SPH

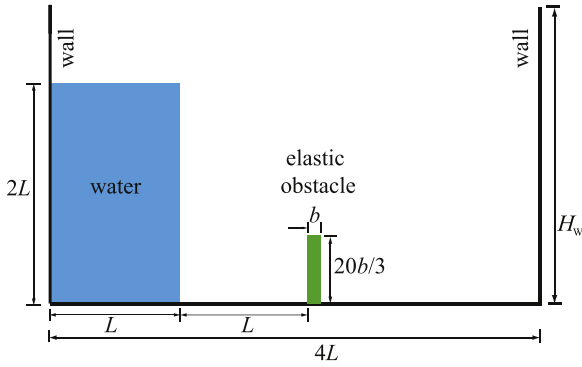**Fig. 17.** Pressure contour: (a) ICFEMP; (b) vp-ICFEMP; (c) SPH.

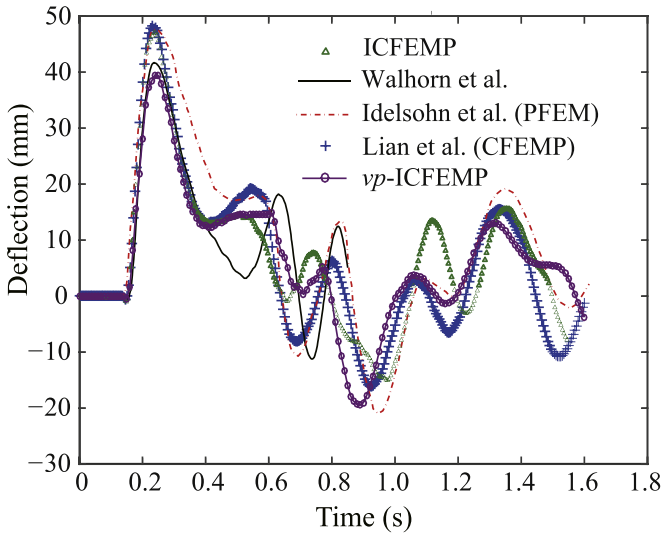**Fig. 18.** A water column impact on an elastic obstacle.

Fig. 19. Time history of the horizontal displacement at the upper left corner of the obstacle.

for both columns. As soon as the flap is taken away, elastic wave will propagate through the water columns. For $t < 10$ ms, the analytical solution is

$$p(x,t) = \begin{cases} 1000 & x < 0.5 - ct \\ 100 & x > 0.5 + ct \\ 550 & \text{otherwise} \end{cases}$$

The cell size of 1 mm and the particle spacing of 0.5 mm are employed to discretize the water columns. The dimensionless constants of artificial bulk viscosity $c_0 = 1.5$ and $c_1 = 0.06$ are chosen. The pressure distribution obtained by different numerical methods at $t = 5$ ms are compared with the analytical solution in Fig. 6. Despite the artificial bulk viscosity, the numerical oscillations occur near the two shock fronts in the MPM. In the vp-MPM without the slope limiter, the numerical oscillation is smoothed significantly except in the region near the shock front. The limiting technique further suppresses the oscillation in the region near the shock front.

To examine the mesh convergence of the linear vp-MPM, cell sizes of 1, 2 and 4 mm are investigated. The particle spacing is kept at half of the cell size. To quantify the errors, the following pressure error norm is employed

$$E = \int_\Omega |\widetilde{p}(x) - p(x)| \mathrm{d}\Omega = \sum_p |\widetilde{p}(x_p) - p(x_p)| V_p \qquad (39)$$

where $\widetilde{p}(x)$ represents the pressure obtained by the numerical method and $p(x)$ signifies the analytical pressure evaluated at posi-

tion x. Fig. 7 plots the logarithm of the error E versus the logarithm of the cell size h.

The MPM can be considered as a Lagrangian FEM with particle quadrature, so the optimal displacement/velocity convergence rate is 2 and the optimal pressure convergence rate is 1. Because the particle quadrature is not optimal, the pressure rate of the MPM is less than 1. Fig. 7 shows that the observed convergence rate of the standard MPM is 0.84 whilst that of vp-MPM is 0.65. Although the convergence rate of vp-MPM is lower than that of the standard MPM due to the artificial dissipation induced by the slope limiter, the vp-MPM predicts a much smoother pressure field and is much more accurate than the standard MPM.

5.2. Dam break

The 2D dam break problem studied experimentally by Zhou et al. [30] and Lobovsky et al. [31] is simulated in this subsection. A schematic drawing of the problem is shown in Fig. 8. Before the test, water with a depth $h_0 = 600$ mm was stored in the reservoir area on the left side of the flap. At $t = 0$, the flap was lifted quickly and the water crashes into the flow area due to the gravity. The initial tank has a length $l_0 = 1200$ mm. P_1 denotes the location of a pressure sensor. The density ρ, viscosity μ and gravity g are 1000 kg/m^3, 1.01×10^{-3} Pa·s and 9.8 m/s^2, respectively. In order to keep the surface of water smoothed, it is assumed that the water can sustain a tension of 6kPa before separation. The water domain is discretized by 28,800 particles with particle spacing 5 mm and background grid cell size 20 mm. The artificial sound speed $c = 50$ m/s is used in this example. The free-slip boundary condition is imposed on all solid walls. To eliminate the cell-crossing error, the $v - p$ formulation is incorporated into GIMP (vp-GIMP). For comparison, this example is also simulated by vp-MPM with/without a slope limiter, WCGIMP and WCMPM.

The following non-dimensional parameters are defined to quantify the results

$$T = t\sqrt{\frac{h_0 g}{l_0^2}}, \quad L(T) = \frac{l(T)}{l_0}, \quad P(T) = \frac{p(T)}{\rho g h_0}$$

where l is the location of the wave front and p is the pressure.

A sequence of snapshots predicted by the WCGIMP and vp-GIMP are compared in Fig. 9. Although the free surface profiles obtained by both methods are very similar at the beginning, non-physical fluid configuration evolves gradually in the WCGIMP. The free surface seems to be unstable as water flows. Moreover, there is a significant difference in the pressure distributions predicted by the two methods. At the beginning, hydrostatic pressure obtained by both methods is close to linear along the vertical direction. However, the pressure obtained by the WCGIMP soon shows high frequency oscillations as the water flows. Although the GIMP can eliminate the cell-crossing error, it can not reduce the numerical oscillation or mitigate the volumetric locking in the weakly compressible problems. In comparison, the pressure distribution obtained by the $v - p$ GIMP is always stable and the free surface profiles are reasonable during the whole process.

The non-dimensional displacements of the wave front obtained by the WCMPM, WCGIMP and vp-GIMP are compared in Fig. 10 with the experimental data of Lobovsky [31]. Meanwhile, the numerical results obtained by the SPH [32] and iMPM [9] are also plotted in Fig. 10 for reference. At the beginning, the experimental wave front is a slightly faster than the predicted wave fronts. After a while, the predicted wave fronts catch up and finally exceed the experimental one. The difference between experimental and predicted wave fronts may be due to several factors in the experiment, such as the flap removal speed and development of turbulence near the water front which causes the delay of the
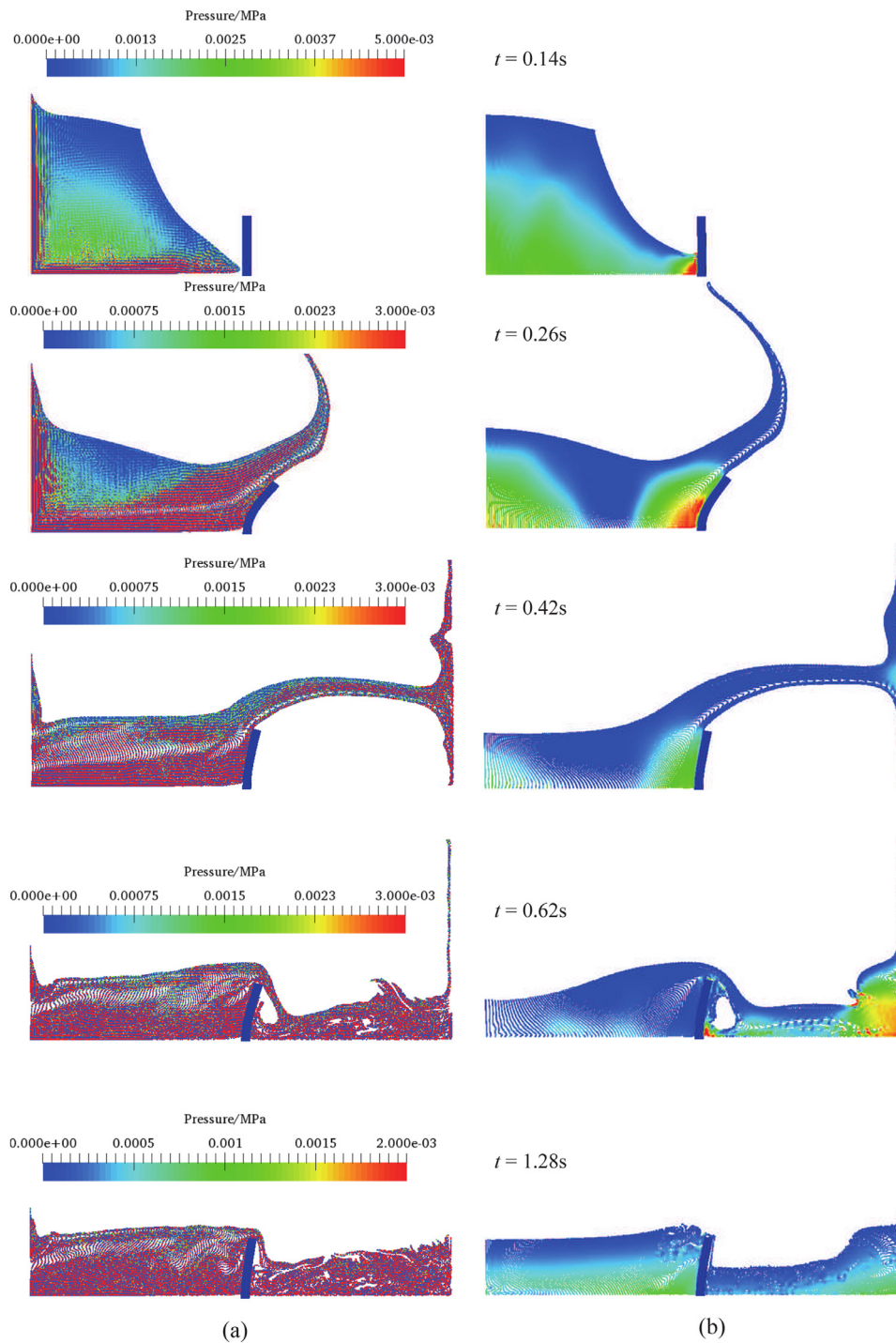
Fig. 20. The deformation of the obstacle and the free surface profile obtained by (a) the ICFEMP and (b) the *vp*-ICFEMP at different times.

downstream motion [9]. The predictions of *vp*-GIMP are the closest to the experimental results.

The pressures at the sensor location P_1 predicted by the *vp*-GIMP with/without a limiter, WCMPM, WCGIMP, SPH and iMPM are compared with the experimental data reported by Zhou et al. [30] in Fig. 11. The results obtained by the *vp*-GIMP and GIMP agree with the experiment data reasonably. On the other hand, the WCMPM shows severe numerical oscillation because of the cell-crossing error. Due to the weakly compressible EOS, the pressure oscillation still exists in the *vp*-GIMP, GIMP and SPH. The delay of

the second pressure peak at $T \simeq 3$ in the numerical methods might be due to the air in the cavity which has not been taken into account in the simulations. Comparing the pressure history obtained by the *vp*-GIMP with and without a limiter shows that the limiter is able to suppress the pressure oscillation near the first pressure peak which corresponds to the shock front.

Note that the time oscillation in pressure may be induced by several facts, including the partial oscillation in pressure, the explicit time integration, and the weak compressible EOS. However, the proposed *vp*-MPM only eliminates the checkerboard pattern

spatial oscillation in pressure induced by the volumetric locking. Thus, the time evolution of the pressure obtained with vp-MPM in Fig. 11 still shows oscillations.

In this example, the vp-MPM and vp-GIMP cost about 80% and 25% higher than the WCMPM and WCGIMP, respectively, due to the extra smoothing procedure in the $v - p$ formulation. Although the generalized interpolation is employed to integrate the nodal force in the vp-GIMP, the standard C^0 interpolation is still used to smooth the particle pressure which is considerably more efficient than the generalized interpolation employed in the vp-MPM. Thus, the extra cost by the vp-GIMP is lower than that of the vp-MPM. However, the total cost by the vp-GIMP is about two times of the vp-MPM.

5.3. Free falling of the wedge

It is a great challenge to simulate the free surface and moving solid bodies together. A wedge falling into water is simulated to investigate the capacity of vp-ICFEMP method for predicting flow phenomena. The velocity variation of the wedge depends on the interaction between the wedge and the surrounding fluid. This problem has been studied by using different methods, such as the level set immersed boundary method (IBM) [33] and the incompressible SPH (ISPH) method [34]. Zhao et al. also conducted an experiment [35], in which the wedge has a breadth of 500 mm, V-shaped section with a 30° dead-rise angle, as shown in Fig. 12. The total weight is 241 kg. The tank has a width of 2 m and depth of 1 m. It is fitted with piezoresistive pressure cells of diameter 4 mm (P1–P5 in Fig. 12). The vertical motion is the only degree of freedom allowed to the wedge in this experiment. The vertical velocity was obtained using an optical sensor. All the numerical methods employed a two dimensional model for this problem.

The problem is assumed to be plane strain in the simulation. The wedge is modeled as rigid body, while the water is modeled by the null material with incompressible EOS. The artificial sound speed is chosen as 50 m/s to increase time step size and avoid the oscillation of pressure [37]. The water is assumed to be unable to sustain tension. The acceleration of gravity is taken to be $g = 9.81 \text{ m/s}^2$. The initial velocity of the wedge falling into water is $v_0 = -6.15$ m/s. The average finite element sizes of the wedge is set to 10 mm. The sizes of the background grid cell are set to 5 mm, while the particle space is 2.5 mm. The whole model consists of 320,000 particles for water, and 390 elements for the wedge.

Fig. 13 plots the time history of the falling velocity of the wedge obtained by different methods. Both the IBM and ISPH assume the fluid as incompressible, while the ICFEMP and vp-ICFEMP assume the fluid as weakly compressible. Before $t = 0.017$ s, the predictions given by ICFEMP, vp-ICFEMP and IBM agree well with experiment data. However, the velocity is over-predicted after that which might be caused by the artificial compressibility of the weak compressible EOS. The results obtained by the ISPH fit the experiment data well in the whole falling process.

In order to investigate the mesh convergence of the vp-ICFEMP method, this problem is studied with the background cell size of 2.5 mm, 5 mm and 10 mm, respectively. The vertical velocities of the wedge at $t = 0.02$ s obtained with different cell sizes are listed in table 1. The results obtained by the vp-ICFEMP are a little larger than those obtained by the ICFEMP. As the cell size decreases, the vertical velocity become smaller. The converged vertical velocity obtained by the vp-ICFEMP is about 0.1 m/s smaller than that of the experiment.

The following non-dimensional parameters are defined to evaluate the results

$$P^* = \frac{P - P_0}{0.5\rho V^2(t)}, Z^* = \frac{Z}{Z_W}$$

Table 1
The vertical velocity at $t = 0.02$ s.

Cell size	Experiment	ICFEMP	vp-ICFEMP
2.5 mm	5.05 m/s	4.89 m/s	4.91 m/s
5 mm	–	4.90 m/s	4.92 m/s
10 mm	–	4.91 m/s	4.94 m/s

where P represents the local fluid pressure, $P_0 = 0$ denotes the air pressure, $\rho = 1000 \text{ kg/m}^3$ is the density of water, $V(t)$ is the vertical velocity of the wedge obtained by Zhao's experiment, Z is the vertical coordinate on the wedge surface, and Z_W is the absolute value of the vertical displacement. Besides, Z_K and Z_D represent the vertical coordinate of the keel and the draft of the body, respectively.

The pressure results obtained by different numerical methods are compared with Zhao's analytical and experimental data at three given instants, and the time starts when the wedge touches the free surface. Figs. 14, 15 and 16 show instants at $t = 0.00435$ s, $t = 0.0158$ s and $t = 0.0202$ s, respectively. The background grid size of 5 mm is used. The red circles on the figures represent the experiment data.

At $t = 0.00435$ s, the analytical results fit the experiment results very well. The pressure results given by the SPH agree with the analytical solution, however the peak at P2 is lower. The results given by the vp-ICFEMP also agree with the analytical solution reasonably except that at the keel, which is a bit lower. Compared with the vp-ICFEMP, the pressure obtained by the ICFEMP method exhibits obvious oscillations, as shown in Fig. 14.

At $t = 0.0158$ s, the experiment data shows that the lowest value appears at P3, while the highest value appears at P5, which is different from the analytical and SPH results. Unlike the analytical and SPH, the pressure results obtained by the vp-ICFEMP is close to the experiment, however the peak value is a bit lower. The ICFEMP agree with the experiment data reasonably, though the pressure oscillation exists.

At $t = 0.0202$s, the pressure results of the experiment are obviously lower than any other methods. ICFEMP shows the closest result to the experiment despite its oscillation. The analytical solution and vp-ICFEMP perform similarly, while SPH performs the worst result.

From all the three pressure distribution in Fig. 14 ∼ 16. ICFEMP fits the experiment best without regard to its oscillation. vp-ICFEMP efficiently suppresses its oscillation and performs very well. SPH show some defects in $t = 0.0158$ s and $t = 0.0158$ s comparing with the other two formulations.

The pressure contours at different moments are plotted in Fig. 17. The pressure contours and the surface profiles given by the vp-ICFEMP and ICFEMP method agree well with those given by the SPH. However, the pressure results obtained by the ICFEMP show obvious numerical oscillation.

5.4. Water impact on an elastic obstacle

The third example is a FSI problem studied by different numerical methods including the PFEM[38], CFEMP[5] and ICFEMP[8]. As shown in Fig. 18, a water column will collapse through an elastic obstacle to the right wall due to the gravity. In the figure, $L = 146$ mm, $b = 12$ mm and the distance from the obstacle to the water column is L.

The water column will collapse freely under the gravity acceleration of $g = 9.8 \text{ m/s}^2$ and the air effect will be ignored. The flexible obstacle with Young's modulus $E = 1$MPa, density $\rho = 2500 \text{ kg/m}^3$ and Poisson's ratio $v = 0$ is simulated by the FEM. The water column is simulated by the vp-GIMP with weakly compressible EOS ($\rho = 1000 \text{ kg/m}^3$, $c = 50$ m/s). To keep the surface of water smooth,

it is assumed that the water can sustain a tension of 6kPa before separation. Both the grid cell size and the finite element size are taken to be 4 mm whilst the particle spacing is 1 mm. The whole model consists of 42,720 particles for the water and 60 elements for the obstacle. The generalized interpolation is also employed in this example.

The time history of the horizontal deflection at the upper left corner of the obstacle predicted by the vp-ICFEMP are compared with other available results in Fig. 19. The present method agrees with the CFEMP, ICFEMP and PFEM reasonably well. The first peak value occurring at around 0.22 s predicted by the vp-ICFEMP is a little lower than other methods due to the dissipation introduced by the $v - p$ formulation and the slope limiter.

The deformation of the obstacle and the free surface profile at five different time instants obtained by the ICFEMP and vp-ICFEMP are shown in Fig. 20. The results of the ICFEMP show non-physical surface profiles whereas the pressure distributions suffer from high frequency numerical oscillations. The particles near the left side seem to be dragged by the left wall, which are mainly resulted from the volumetric locking. By employing the $v - p$ formulation, the surface profile and the pressure distribution become much more reasonable. The FSI simulation costs 169 min for the ICFEMP and 224 min for the vp-ICFEMP. The extra 33% computing time is consumed in the smoothing procedure, which is acceptable in view of the significant improvement in the prediction.

6. Conclusion

In weakly compressible problems, the Hu-Washizu multi-field variational principle with independently assumed displacement/velocity, strain and stress was employed to mitigate the volumetric-locking. Compared with the standard MPM, 12 extra nodal/particle variables are required to be constructed which significantly increase the computational cost. Using a two-field variational principle in which the velocity v and the pressure p are the independent variables is more convenient[22] for nearly incompressible problems. The v-p formulation requires less calculation than the Hu-Washizu multi-field formulation because only one extra variable (pressure) needs to be constructed. Employing a slope limiter in the present vp-MPM can successfully suppress the spurious pressure oscillation which occurs at the interface of discontinuity due to large pressure gradient difference between the control volumes of grid nodes. Furthermore, the generalized interpolation is employed to alleviate the cell-crossing error. Numerical studies show that the vp-MPM and vp-GIMP greatly improve the predicted pressure distribution and the fluid surface profile. Compared with the GIMP, only about 30% extra cost is required by the vp-GIMP for the smoothing procedure. The wedge falling and water impact simulation show the applicability of the vp-ICFEMP to fluid–structure interaction problems.

References

[1] Sulsky D, Chen Z, Schreyer HL. A particle method for history-dependent materials. Comput Methods Appl Mech Eng 1994;118(1–2):179–96.
[2] Sulsky D, Zhou SJ, Schreyer HL. Application of a particle-in-cell method to solid mechanics. Comput Phys Commun 1995;87(1–2):236–52.
[3] Zhang X, Chen Z, Liu Y. The material point method - A continuum-Based particle method for extreme loading cases. Academic Press; 2016.
[4] Li JG, Hamamoto Y, Liu Y, Zhang X. Sloshing impact simulation with material point method and its experimental validations. Comput Fluids 2014;103:86–99.
[5] Lian YP, Zhang X, Liu Y. Coupling of finite element method with material point method by local multi-mesh contact method. Comput Methods Appl Mech Eng 2011;200:3482–94.
[6] Lian YP, Liu Y, Zhang X. Coupling of membrane element with material point method for fluid-membrane interaction problems. Int J Mech Mater Des 2014;10:199–211.
[7] Mast CM, Mackenzie-Helnwein P, Arduino P, Miller GR, Shin W. Mitigating kinematic locking in the material point method. J Comput Phys 2012;231(16):5351–73.
[8] Chen ZP, Qiu XM, Zhang X, Lian YP. Improved coupling of finite element method with material point method based on a particle-to-surface contact algorithm. Comput Methods Appl Mech Eng 2015;293:1–19.
[9] Zhang F, Zhang X, Sze KY, Lian Y, Liu Y. Incompressible material point method for free surface flow. J Comput Phys 2017;330:92–110.
[10] Zhang F, Zhang X, Sze KY, Liang Y, Liu Y. Improved incompressible material point method basedon particle density correction. Int J Comput Method 2017(11):1850061.
[11] Kularathna S, Soga K. Implicit formulation of material point method for analysis of incompressible materials. Comput Methods Appl Mech Eng 2017;313:673–86.
[12] Bardenhagen S, Kober E. The generalized interpolation material point method. Comput Model Eng Sci 2004;5(6):477–96.
[13] Wallstedt PC, Guilkey JE. An evaluation of explicit time integration schemes for use with the generalized interpolation material point method. J Comput Phys 2008;227(22):9628–42.
[14] Sadeghirad A, Brannon RM, Burghardt J. A convected particle domain interpolation technique to extend applicability of the material point method for problems involving massive deformations. Int J Numer Methods Eng 2011;86(12):1435–56.
[15] Sadeghirad A, Brannon RM, Guilkey JE. Second-order convected particle domain interpolation (CPDI2) with enrichment for weak discontinuities at material interfaces. Int J Numer Methods Eng 2013;95(11):928–52.
[16] Zhang DZ, Ma X, Giguere PT. Material point method enhanced by modified gradient of shape function. J Comput Phys 2011;230(16):6379–98.
[17] Steffen M, Kirby RM, Berzins M. Analysis and reduction of quadrature errors in the material point method (MPM). Int J Numer Methods Eng 2010;76(6):922–48.
[18] Gan Y, Sun Z, Chen Z, Zhang X, Liu Y. Enhancement of the material point method using b-spline basis functions. Int J Numer Methods Eng 2018;113(3):411–31.
[19] Beuth L, Wieckowski Z, Vermeer PA. Solution of quasi-static large-strain problems by the material point method. Int J Numer Anal Methods Geomech 2011;35(13):1451–65.
[20] Sulsky D, Gong M. Improving the material-Point method. Springer International Publishing; 2016.
[21] Washizu, Kyichir. Variational methods in elasticity and plasticity. Pergamon Press; 1975.
[22] Zienkiewicz OC, Taylor RL, Zhu JZ. The Finite Element Method: Its Basis and Fundamentals. Butterworth-Heinemann; 2013.
[23] Morris JP, Fox PJ, Zhu Y. Modeling low Reynolds number incompressible flows using SPH. J Comput Phys 1997;136(1):214–26.
[24] Belytschko T, Liu WK, Moran B. Nonlinear finite elements for continua and structures. John Wiley & Sons Inc.; 2014.
[25] Bathe K-J. Finite element procedures. Prentice Hall; 2006.
[26] Van Albada G, Van Leer B, Roberts Jr W. A comparative study of computational methods in cosmic gas dynamics. Astron Astrophys 1982;108:76–84.
[27] Roe PL. Characteristic-based schemes for the euler equations. Annu Rev Fluid Mech 1986;18(1):337–65.
[28] Van Leer B. Towards the ultimate conservative difference scheme. J Comput Phys 1997;135(2):229–48.
[29] Barth T, Jespersen D. The design and application of upwind schemes on unstructured meshes. AIAA paper 1989:89–0366.
[30] Zhou Z, Kat JD, Buchner B. A nonlinear 3-d approach to simulate green water dynamics on deck. In: Proceedings of the 7th international symposium on numerical ship hydrodynamics; 1999.
[31] Lobovsky L, Botia-Vera E, Castellana F, Mas-Soler J, Souto-Iglesias A. Experimental investigation of dynamic pressure loads during dam break. J Fluids Struct 2014;48:407–34.
[32] Hughes JP, Graham DI. Comparison of incompressible and weakly-compressible SPH models for free-surface water flows. J Hydraul Res 2010;48(sup1):105–17.
[33] Zhang Y, Zou Q, Greaves D, Reeve D, Hunt-Raby A, Graham D, et al. A level set immersed boundary method for water entry and exit. Commun Comput Phys 2010;8(2):265–88.
[34] Shao SD. Incompressible SPH simulation of water entry of a free-falling object. Int J Numer Methods Fluids 2009;59:91–115.
[35] Zhao R, Faltinsen O, Aarsnes J. Water entry of arbitrary two-dimensional sections with and without flow separation. In: Proceedings of the 21st symposium on naval hydrodynamics; 1997.
[36] Oger G, Doring M, Alessandrini B, Ferrant P. Two-dimensional SPH simulations of wedge water entries. J Comput Phys 2006;213(2):803–22.
[37] Morris JP, Fox PJ, Zhu Y. Modeling low Reynolds number incompressible flows using SPH. J Comput Phys 1997;136(1):214–26.
[38] Idelsohn SR, Marti J, Limache A, Onate E. Unified lagrangian formulation for elastic solids and incompressible fluids: application to fluid-structure interaction problems via the PFEM. Comput Methods Appl Mech Eng 2008;197:1762–76.